A Novel Radiogenomics Framework for Genomic and Image Feature Correlation using Deep Learning

Shuai Li[1], Hongze Han[1], Dong Sui [1,2,*], Aimin Hao[1]
[1]*Beihang University*
[2]*Beijing University of Civil Engineering and Architecture*
suidongcs2016@gmail.com

Hong Qin[1]
[1]*Stony Brook University (SUNY at Stony Brook)*
Stony Brook, New York 11794-2424
qin@cs.stonybrook.edu

***Abstract*—Precision medicine still remains to be a prevalent treatment strategy which has been continuously pushed forward by the upcoming targeted therapies. To improve the precision and quantitative level, researches in radiomics and radiogenomics have devoted much of their endeavors to transform digital standard of medical images to mineable high-dimensional data by way of extracting mathematically quantitative features. However, most of the prior efforts could not effectively combine multi-source medical data sets together to generate satisfactory results and then visualize diagnoses by unifying low level features from images and other sources. In this paper, we design a novel and meaningful framework in order to map the features between medical images and gene expression profiles and quantify their correlations. To ameliorate, we take full advantage of deep learning methods, and characterize the lung cancer clinically at both genome and image levels. Our newly-devised protocol could give a strong association between gene and tumor growth statues, furthermore, it could provide cogent visual results for clinical research directly. The research presented in this paper could provide more comprehensive characterizations of tumor phenotypes, statues, and outcomes. As a result, it may be noted that, all of our prior efforts could contribute to the bigdata analysis for biomarker signatures, images, and "Omics".**

***Index Terms*—Radiomics; Radiogenomics; Deep Learning; Genomics Biomarker**

I. Introduction and Motivation

In the past decades, patients diagnosed with lung cancer and its-related deaths have been increasing [1]. Now it is apparent that, lung cancer have already become a leading cause of cancer-related deaths all over the world, with up to 70% of lung cancer diagnoses being made after the onset of symptoms from advanced local or metastatic disease. But the survival rate is only about 50%, only when its diagnoses could be localized. Unfortunately, only less than 20% of these patients are diagnosed at very early stages. This gives rise to lots of imaging studies and surgical excisions which are costly and unnecessary. Thus, affordable and accurate cancer screening methods are highly demanded with significant impacts [2].

Precision medicine is gaining popularity for providing customized or personalized healthcare, and quantitative imaging has been contributing to significant improvement of the diagnosis procedures [2]. Traditionally, radiology and image-guided intervention have been dealing with diagnosis and have provided anatomical abnormality information. But all of these approaches have to make body wounds with pain suffering and long recovery time for patients. To conquer these shortcomings, radiomics can extract image features and sub-visual characteristics from radiologic images, and provide unique potential for making lung cancer screening more rapidly and accurately using the state-of-the-art machine learning techniques. Thus, by improving the practice of qualitative and quantitative analysis, we could expect to enhance the prognosis prediction and response to certain therapies. Apart from these, some radiogenomics researchers have demonstrated that some image features have even been correlated with genomic alterations within tumor DNA [2]. In addition, the features could identify the presence of specific alterations in biological pathways, which in turn affect the management and healthcare outcome of patients [3]. In this paper, we develop a deep learning centric radiogenomics framework to map the image features and gene expression profile data. Our salient contributions are as follows:

- We propose a deep learning based framework for tumor biological features and information extracted from tumor region (TR) correlation between image and gene level, and the results demonstrate strong associations between genome data in expression profiles and tumor growth information in CT/PET images.
- We combine the gene expression and tumor growth information into autoencoder networks to correlate the image and genomic features.
- We use genome level information to generate a cogent visual result of tumor status in generated CT images, and the results could demonstrate a strong association between gene expression and tumor anatomy structure.

II. Related Works

In the fields of radiomics and radiogenomics, qualitative and quantitative image features are extracted from medical images to obtain diagnostic, predictive, or prognostic information. These give rise to the development of novel imaging signatures and feature extraction methods, which improve diagnostic and prognostic performance in various oncologic applications. In this part, we review recent achievement in this field, and more details are presented below.

* Corresponding author Dong Sui, email: suidongcs2016@gmail.com.

978-1-5386-5488-0/18/$31.00 ©2018 IEEE

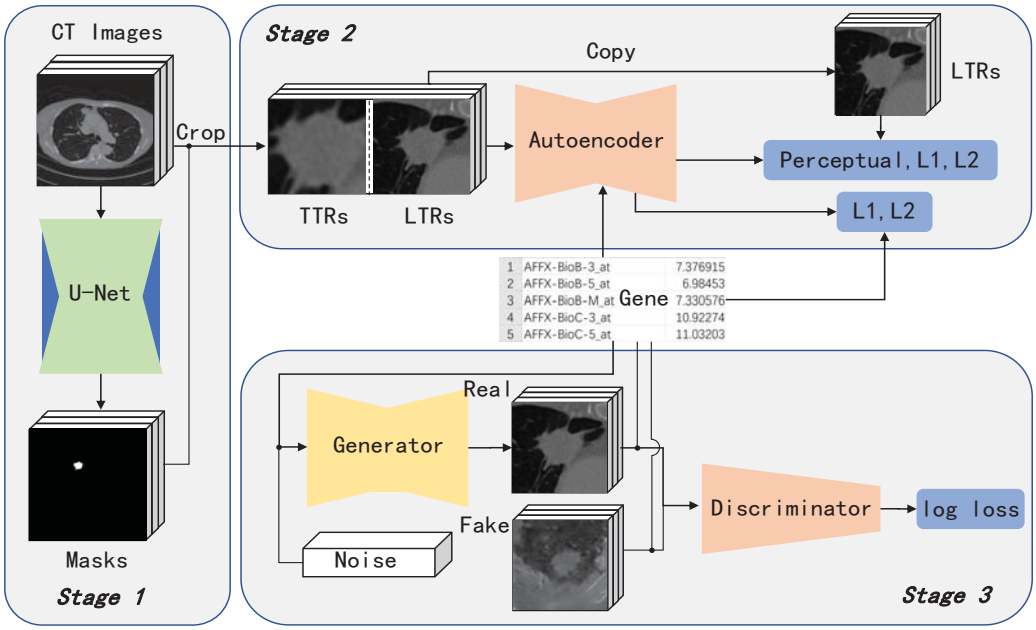

Fig. 1. The work flow of our proposed framework. Stage 1: Tumor detection. Stage 2: Gene and image mapping. Stage 3: Synthetic tumor region Generation.

A. Radiomics and Radiogenomics Approaches

Traditionally, radiomics and radiogenomics involve four steps: image acquisition, lesion segmentation, feature extraction and model validation. Following these steps, Aerts *et al.* propose a quantitative strategy to map the low level image features and gene expression profile data, and provide an unprecedented opportunity to improve decision-support in cancer treatment at low cost [7]. In their work, the correlation between computed tomography (CT) images and genome data can reflect grate clinical significance and survival time of patients [33]. Coroller *et al.* build a correlation between image features and clinical data to predict distant metastasis in lung adenocarcinoma [6]. Additionally, Gevaert *et al.* propose a protocol by mapping semantic features with genome data, and get a model with an area under the receiver operating characteristic curve (AUC) of 65% or greater [31]. This shows that purely CT images information can originally predict the overall clinical status of a patient. Abdollahi *et al.* also predict sensorineural hearing loss successfully in the same way on cochlea CT radiomics [25]. Besides these, more researches exhibit the great connection and correlation between image features and genomic data. All of these works demonstrate that quantitative information from the image features plays predominant position in the radiomics and radiogenomics approaches. These quantitative image features from CT including intensity, shape, texture and wavelet. In details, the intensity features contain the distribution of pixel intensities within the CT image through commonly used and basic metrics. The shape features contain compactness, area, diameter, etc.. The texture and wavelet features are obtains through multi convolutional operators and wavelet transform respectively. There are some semantic features given by human depend on

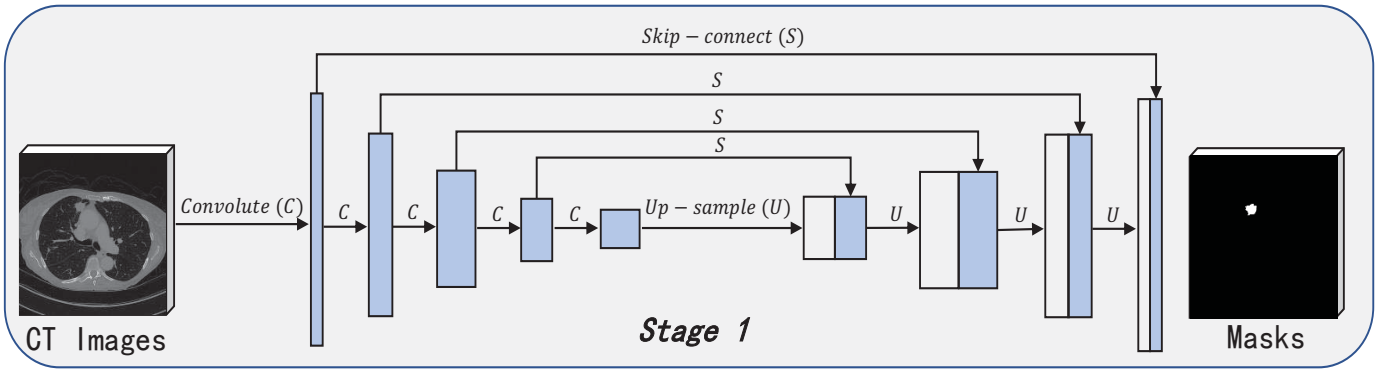

Fig. 2. U-net architecture for tumor segmentation.

different task. The above methods establish a strong correlation between image features and genomic information or clinical data, which verifies the possibility of lesions growth prediction from the gene level alone.

B. Deep Learning for Radiological Analysis

Radiomics and deep learning (DL) are hot issues in the field of medical imaging [6]. As a data driven protocol with few interaction with people, DL has been employed for medical image data analysis tasks, such as in CT, Magnetic Resonance (MR), and Positron Emission Tomography (PET). It can provide informative information about diagnosis, patients' outcome, tumor phenotypes, and the gene-protein signatures in lung cancer treatments and prediction [6]. Some recent progress is as followed.

Convolutional neural networks (CNNs) have achieved great success in computer vision community, especially in medical imaging analysis. Many researchers followed this trend and proposed to utilize various CNNs for learning feature representations in the application of lung node and mass segmentation [3]–[5]. Autoencoder is a popular encoder-decoder architecture. It can give an auto-encoding complex anatomical prior in medical imaging segmentation task which eliminates the burden of providing paired example segmentations [14], [18]. Xu *et al.* propose an approach of nuclei detection on breast cancer histopathology images, which uses the hidden nodes' output of autoencoder to detect and classify nuclei of breast cancer [18]. This indicates that high-level features of autoencoder can almost describe the input image. Gondara applies the denoising autoencoder with pixel missed images as inputs for noise reduction in medical images [19], and shows the repair capability of autoencoder through convolutional decoder.

The U-Net architecture achieves excellent performance on different biomedical segmentation applications. Dong *et al.* use the U-Net based deep convolution networks to fulfill the fully automatic brain tumor detection and segmentation task [10]. Han *et al.* show that the alternative U-Net variants such as dual frame and the tight frame U-Nets satisfy the so-called frame condition which make them better for effective recovery of high frequency edges in sparse view-CT [11]. Jin *et al.* propose a novel deep U-Net-based algorithm for solving ill-posed inverse problems [12]. Han *et al.* develop a novel deep residual learning approach based on U-Net for sparse view CT reconstruction [13].

The Generative Adversarial Nets (GANs) have the ability to generate the results as expected. GAN consists of two adversarial models including a generative model G and a discriminative model D. G captures the data distribution and D estimates the probability that a sample came from the training data rather than G. Both G and D could be a non-linear mapping function, like a multi-layer perception [16]. The objective function of the whole model during training steps is:

$$\begin{aligned} \min_G \max_D V(D,G) = \mathbb{E}_{x\sim p_{data}(x)}[logD(x)] \\ +\mathbb{E}_{z\sim p_z(z)}[log(1-D(G(z)))], \end{aligned} \tag{1}$$

where x is input data of model, $p_z(z)$ is input noise variable.

Recently, GAN frameworks have been applied to several medical imaging problems, including creating translation of label-to-image, mask-to-image or medical cross modality. Dai *et al.* train GAN to segment lung fields and heart in chest X-ray images [21]. Nie *et al.* train a patch-based GAN to construct transition between brain CT images and the corresponding MRI images, and suggest an auto-context model to refine image [22]. Ben-Cohen *et al.* also introduce a cross modality image generation using GAN, from abdominal CT image to a PET scan image that highlights liver lesions. Some studies have been inspired by the GAN method for image inpainting [24]. Schlegl *et al.* train GAN with healthy patches of the retinal area to learn the data distribution of healthy tissue [23]. Unfortunately, the TR usually adhere or near to some certain structures in lung fields, and the generated results have no anatomy prior by using GAN with a random input. Conditional Generative Adversarial Nets (CGAN) have the advantage of extra information appended [20]. Compared to GAN, it gives a condition y in generation process and leads to certain output:

$$\begin{aligned} \min_G \max_D V(D,G) = \mathbb{E}_{x\sim p_{data}(x)}[logD(x|y)] \\ +\mathbb{E}_{z\sim p_z(z)}[log(1-D(G(z|y)))]. \end{aligned} \tag{2}$$

Dakai *et al.* propose an architecture, which uses the mask of lung nodule to generate a synthetic lung nodule under the supervision of ground truth image [36]. Dong *et al.* propose an architecture, which predicts the translation parameters of Altas to generate the mask volume of Left Ventricle (LV) under the supervision of target volume [37]. These researchers indicate CGAN architecture can generate expected medical images.

III. Radiogenomics Correlation and Visual Results Generation

Most recent personalized and precision medicine could tailor medical care to individual need by characterizing molecular heterogeneity, which have become the prominent task in radiogenomics. For example, rapid advances in imaging and genome technologies afford better anatomic resolution and noninvasive biomarker based measurement towards more accurate and effective tumor evaluations. As a study cohort, paired gene expression data and medical images have been leveraging the outcomes of tumor from a closely matched population [31]. Some research works have generated maps that integrate the genomic and image data to gain informative diagnosis results, clinical staging, and treatment planning. Yet most of the prior works use only hand-crafted or computerized features of images, there are few deep learning frameworks for the same task proposed in such context. We devise a deep learning based framework for tumor status correlation between image and gene level, furthermore, we exploit genome level

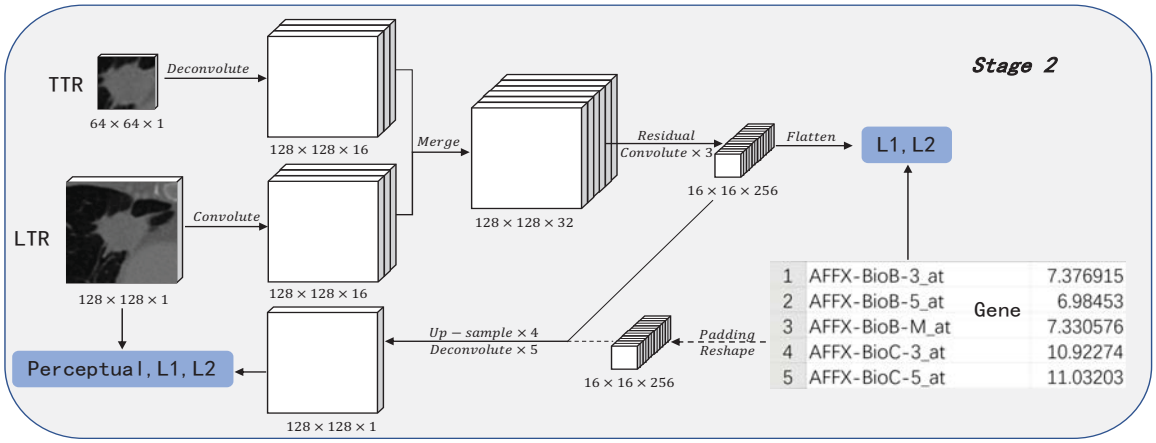

Fig. 3. Illustration of our autoencoder for gene and images mapping. The dashed arrow shows the way that gene enters the decoder of autoencoder for visualization the learning capacity of the encoder.

information to generate a cogent visual result of tumor for possible clinical tests. Towards this goal, in order to map the gene expression profile data and CT image features from Non-Small Cell Lung Cancer (NSCLC), we now introduce the following three steps (see Figure 1). We first use the U-net architecture to detect and crop TR in lung CT images for ROI extraction. Second, the autoencoder is employed to learn the distribution from CT image to gene, and features extracted from the model are clustered with gene to confirm the strong correlation. Finally, CGAN is utilized to transform from the gene features to CT images with provided visual results.

A. Dataset

We choose 2 datasets for the radiogenomics features construction and results evaluation. Dataset Lung3 and NSCLC Radiogenomics are from Cancer Archive [32], [33], cancerous regions in NSCLC are relabeled as masks and binding boxes by doctors.

Lung3: The dataset which contains 89 patients' data. For these patients pretreatment CT scans, gene expression, and clinical data are available. The gene expression data of one patient includes 60607 Log2 normalized intensity values which are generated by RMA algorithm.

NSCLC Radiogenomics: A unique radiogenomic dataset from a NSCLC cohort of 211 subjects. The dataset comprises Computed Tomography (CT), PET/CT images, semantic annotations of the tumors as observed on the medical images using a controlled vocabulary, segmentation maps of tumors in the CT scans, and quantitative values obtained from the PET/CT scans. Additionally, we manually label binary mask of tumor in each series of CT images.

B. Tumor Detection and Segmentation

We use U-Net to perform TR segmentation on NSCLC dataset. We select each CT image which contains a tumor and its binary mask as a paired data. Finally, 2332 paired CT images and masks are got for training and testing. The architecture of U-Net is shown in Figure 2. For details, the U-net has five convolutional blocks in encoder, each of which has two convolution layers with 3×3 kernel size, a batch normalization layer and a maxpooling layer with strides of 2. It also has five convolutional blocks in decoder, each of which has two convolution layers with 3×3 kernel size, a merge layer, a dropout layer and a up-sampling layer. In segmentation, U-net uses $Dice$ loss [9] to measure the contact ratio between predicted mask (PM) and ground truth (GT):

$$Dice = \frac{2|PM \bigcap GT|}{|PM| \bigcup |GT|}, \tag{3}$$

In training step, we change them to Equation 4 for pixel value of P and T are [0,1] and 0,1 separately.

$$Dice = \frac{2\sum_i^N p_i t_i}{\sum_i^N p_i + \sum_i^N t_i + \epsilon}, \tag{4}$$

where p_i is the pixel value in P, t_i is the pixel value in T, N is total number of pixels in an image, and ϵ is a small constant to avoid division by zero.

U-net model is trained for 500 epochs using the Adam optimizer [35] with a learning rate 0.001, which can detect TR from CT image series [35]. Then this pre-trained model is transfered to detect TR in CT images of Lung3 dataset. For the TR detection, to avoid the disturb of other organs, we only choose the CT images which contain lung to detect on Lung3 dataset. Gevaert's work shows that some global features have strong correlation with genome level information [31]. In this context, we use both global and local features in deep learning protocol to construct this correlation. CT image in tight and loose bounding box of tumor are called tight tumor region (TTR) and loose tumor region (LTR) separately, which contains global and local features. To get LTR, we crop the TR at size of (128,128) with tumor centered in each image. To get TTR, we crop the TR and resize it to the size of (64,64), and we get a 636 samples dataset (dataset C). Each sample of C contains a TTR, a LTR and a gene expression data.

C. Correlation of Genomic information and CT image features

Autoencoder can decode image into a series of representation, in this part, we combine these with genomic information for correlation task, our aim is to obtain an encoder which performs as a mapping from image to gene. Let $C = (X_i^t, X_i^l, Y_i)$ be the dataset for training, where X_i^t is the TTR and X_i^l is the LTR from the same CT image, and Y_i is the corresponding gene expression data. Let $h(\cdot)$, $t(\cdot)$ be the encoder and decoder of autoencoder H separately. The predicted gene expression data $\tilde{Y}_i = h(X_i^t, X_i^l; \theta^h)$, where θ^h is weights of h. The decoded LTR $\tilde{X}_i^l = t(Y_i; \theta^t)$, where θ^t is weights of t. The whole autoencoder function can be expressed as:

$$[\tilde{X}^l, \tilde{Y}] = [h(X^t, X^l; \theta^h), t(h(X^t, X^l; \theta^h), \theta^t)]. \tag{5}$$

Thus, the autoencoder has two inputs and two outputs, which can fit the gene expression data and simultaneously ensure that encoder learns the distribution from TR to gene and decoder learns the distribution from gene to TR. We apply the architecture (Figure 3) on Lung3 dataset to map gene and image. While training the autoencoder H, we use perceptual loss [34] and $l_{1,2}$ loss to fit $H(X^l, X_t)$ to X^l:

$$\ell_{feat}^{\phi,j}(\tilde{X}^l, X^l) = \frac{1}{C_j H_j W_j} \parallel \phi_j(H(X^l, X^t)) - \phi_j(X^l) \parallel_2^2, \tag{6}$$

where ϕ is the pre-trained VGG16 CNN model on ImageNet, j is the j th layer in ϕ, here we use the layer named 'block5 conv3', and $C_j H_j W_j$ is feature map of j th layer. $l_{1,2}$ loss combines the l_1 loss and l_2 loss:

$$\begin{aligned} &\ell_{1,2}^{\phi}(\tilde{X}^l, X^l) = \\ &0.5\ell_1(H(X^l, X^t), X^l) + 0.5\ell_2(H(X^l, X^t), X^l). \end{aligned} \tag{7}$$

We use this $l_{1,2}$ loss to fit $\tilde{Y}$ to Y:

$$\begin{aligned} &\ell_{1,2}^{h}(\tilde{Y}, Y) = \\ &0.5\ell_1(h(X^l, X^t), Y) + 0.5\ell_2(h(X^l, X^t), Y), \end{aligned} \tag{8}$$

So the final loss function of H is ℓ^H :

$$\begin{aligned} &\ell^H([X^l, X^t], Y) = \\ &0.25\ell_{feat}^{\phi,j}(\tilde{X}^l, X^l) + 0.25\ell_{1,2}^{\phi}(\tilde{X}^l, X^l) + 0.5\ell_{1,2}^{h}(\tilde{Y}, Y). \end{aligned} \tag{9}$$

To make sure its high mapping capability of the final model H, we choose 127 samples to be validation data and 509 samples to be train data. The samples of train and validation data are from different patients. The ratio of train and validation data is 8:2. We train the model H for 4k epochs using the Adam optimizer [35] with a learning rate 0.001 on train data. We add a padding operator before input of gene to smooth the dimension difference between encoder's output and gene. The padded gene is scaled to [0,1] for letting encoder of H fit gene better.

D. Pathological Visualization

Although, the previous works can give a mathematic demonstration about the correlation between gene and images, and have never highlight a visual results on its pathological situation, which is greatly demanded for prognosis inference. We use gene expression data for LTR generation to visualize the tumor's location and modality in the lung. Symbols X^l, Y are defined in Equation 5, X^l is simplified as X. The noise z is normally distributed as:

$$p_z(z) = N(\mu, \delta), \tag{10}$$

where μ is constant 0, and δ is constant 1. For a CGAN architecture defined as Equation 2:

$$\tilde{X} = G(z|Y), \tag{11}$$

$$valid = D(\tilde{X}|Y), \tag{12}$$

where $\tilde{X}$ is a synthetic TR, and $valid$ is the probability discriminator judges $\tilde{X}$ to be a real TR.

During the adversarial process between G and D, $valid$ will be close to 1. The noise z will be transformed to $\tilde{X}$ by G conditioned by gene Y, and the synthetic TR $\tilde{X}$ will be almost close to real TR. We train CGAN (shows in Figure 4)

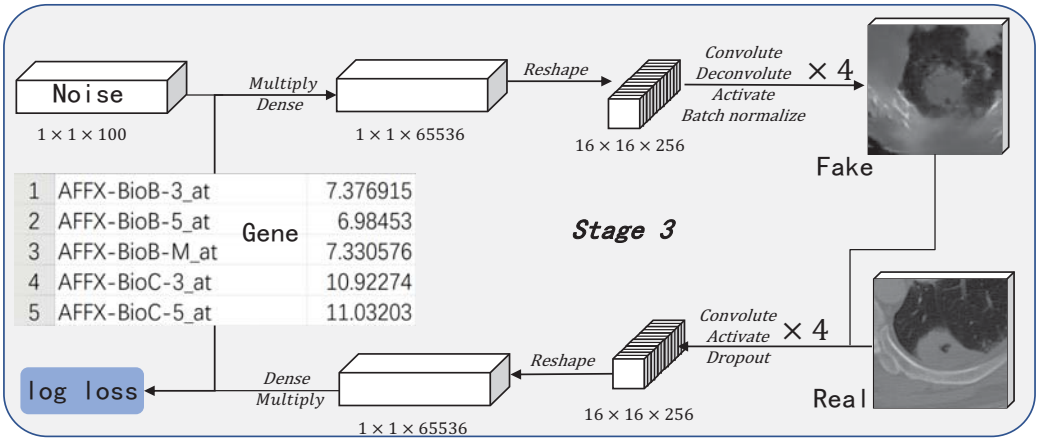

Fig. 4. Illustration of our CGAN architecture. 1) Generator part (top), inputs: noise with length 100 and metagene (clustered from original genes) with length 100, outputs: synthetic TRs; 2) Discriminator part (down), inputs: the real and synthetic TRs (not meanwhile), outputs: label of TRs.

for 20k epochs using the Adam optimizer [35] with a learning rate 0.001 with the noise z and gene as inputs. The synthetic TRs that CGAN predicts using gene are showed in Figure 8.

IV. Results and Discussion

The detection result is shown in Figure 5. The mask in blue indicates the location of tumor, and then TR can be cropped from CT image precisely. Due to the irregular shape and less obvious edge of tumor, the mask can only cover most of tumor. But that is enough to fit the detection task. Meanwhile, the predicted mask can not only give the location, but also the size of the tumor. Our labeled mask cover the implicit edge of tumor, so the predicted mask contains more surrounding information, such as bronchial tube and lung edge, which is crucial in mapping stage.

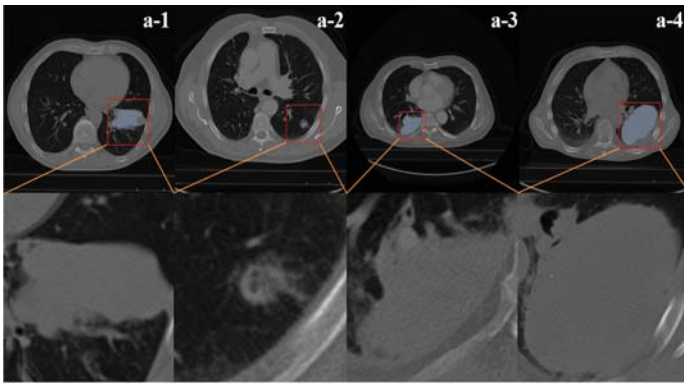

Fig. 5. Tumor segmentation results. Images of row a from a-1 to a-4 are original CT image that each image contains a tumor in blue mask. The red bounding box is the cropped tumor region. Bottom images are the corresponding magnification of tumor regions in Row a.

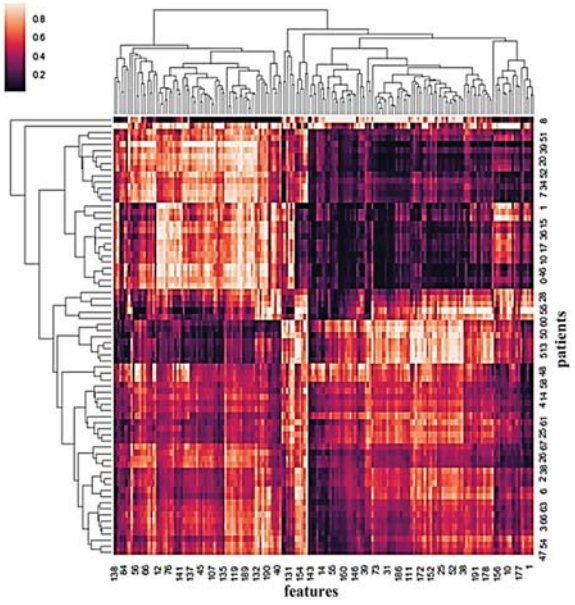

Fig. 6. Cluster results of image features and patients' metagene. The 192 features (partly labeled) are extracted from autoencoder for each patients, and the higher color value indicates the stronger correlation.

In Lung3 dataset, there is only one single biomarker of a patient, this leads to other detection methods like region proposal are not necessary. To sum up, in detection task, the U-net architecture can give location and boundingbox in the meantime efficiently while detecting one single target. It works well in the tumor segmentation task,which promises the effect in next two stages. The mask and binding box permits the following networks can grab critical features from both in and surrounding the tumor, and can also provide more details for feature extraction from cancerous region.

The images that H's outputs are shown in Figure 7. The similarity between autoencoder's outputs (Row a) and encoder's outputs (Row b) can prove the encoder transform the images to the gene expression data successfully. Meanwhile, the similarity between first two rows and ground truth shows the autoencoder fit this task well. Through this stage, layers of encoder can output the features which can be transformed to gene. We compare predicted gene with original gene by multi metrics. The metrics and bias are Mean Average Error (MAE) 4.112E-06, Mean Square Error (MSE) 4.318E-06, Jensen-Shannon (JS) 0.015, Hellinger distance (HD) 0.121, Bhattacharyya Distance (BD) 0.015. These metrics show the bias between predicted gene and original gene (removed the padding part). These values of metrics indicates that H learns the distribution well from CT images.

To construct the correlation between gene and CT images, like Gevaert *et al* [32] do, We cluster the 60607 gene into 100 metagene. Then the metagene and features from the output of first two blocks in H's encoder are clustered. The mapping result is shown in Figure 6. Each row represents the features extracted by our framework with one typical CT TR image of a patient. Each column represents values of the same feature of patients. For each gene, CGAN generates 64 synthetic LTRs in multi forms. Each form indicates the tumor's possible growth state of a patient with specific gene expression data.

Compared with the real tumor region, the obtained visual results from genetic data can directly reflect the lesion information. In Figure 8, the rows from a to c are the synthetic results and the row gt is original TR. Column 1 to 4 shows that the original tumors have clear edge, and similar to synthetic ones generated with paired gene of original tumor. In column 5 and 6, the original tumors' edge is vague for the surrounding bronchus. The synthetic ones are also surrounded by some noise, which is similar to bronchus. Additionally, all the synthetic tumors are generated in the correct locations and the synthetic LTR exhibits an accurate anatomical structure.

V. Conclusion

In this paper, we designed a novel deep learning based framework for computing feature correlation across genome and image levels. The features from tumor images were first mapped to the meta genes, and the clustered features were then used to declare a strong correlation between gene and TR in CT images across the patients. Finally, we built a visualization result from gene to TR. The results were validated by doctors

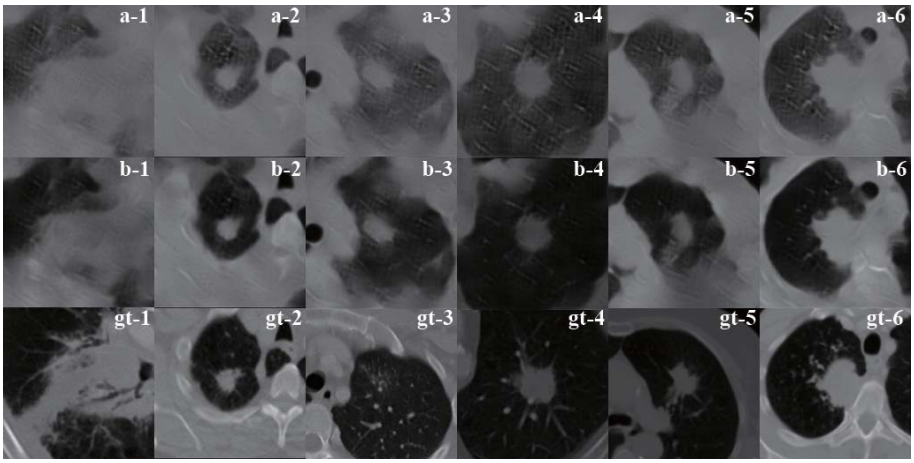

Fig. 7. Outputs of autoencoder. The images from 1 to 6 column are samples of different patients. The row a-1 to a-6 are the output of autoencoder with LTR and TTR as inputs. The row b-1 to b-6 are the output of decoder with genes as input. The row gt-1 to gt-6 are the different original TR from different patients. The process indicates the learning ability of autoencoder from image to gene and from gene to image.

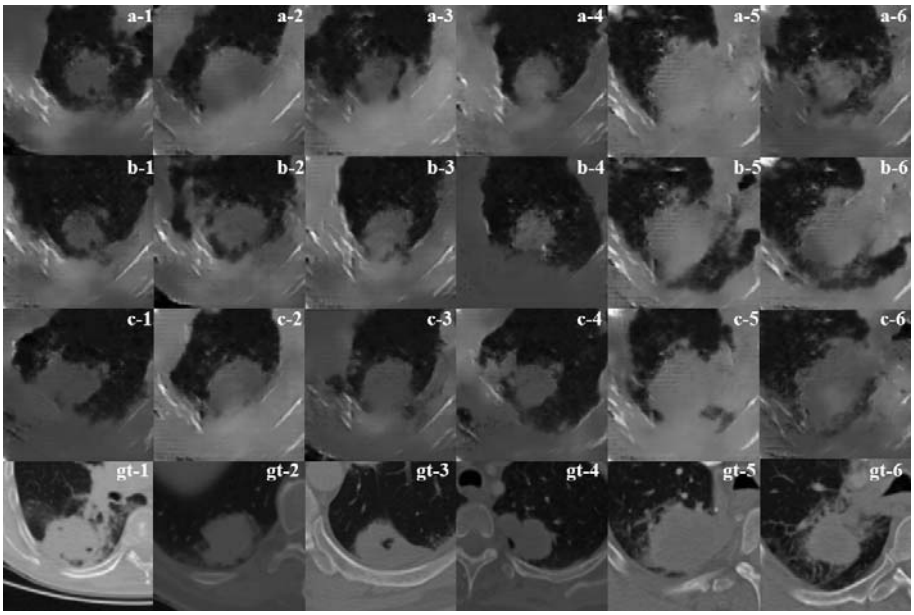

Fig. 8. Synthetic TRs. The row gt is the real TRs from patients 1-6, and row a-c are synthetic TRs using gene that corresponded to real TR in the same column and random noise.

who confirmed that such results were similar to real TRs in clinical settings.

As for possible limitations relevant to the scale and unbalance issues of dataset, the current visual results attained in this paper tend to localize tumor near the lung edges. Since the proposed framework has demonstrated its capability in mapping the gene and tumor status, our future works will be mainly focused on outcomes and living time estimation from concerned cancer patients, and furthermore, data augmentation and new efforts on generative model protocols for precise visual results are of immediate interest to us.

REFERENCES

[1] Fitzmaurice C, Allen C, Barber R M, et al. Global, regional, and national cancer incidence, mortality, years of life lost, years lived with disability, and disability-adjusted life-years for 32 cancer groups, 1990 to 2015: a systematic analysis for the global burden of disease study[J]. JAMA oncology, 2017, 3(4): 524-548.

[2] Thawani R, McLane M, Beig N, et al. Radiomics and radiogenomics in lung cancer: A review for the clinician[J]. Lung cancer (Amsterdam, Netherlands), 2018, 115: 34.

[3] Giger M L, Karssemeijer N, Schnabel J A. Breast image analysis for risk assessment, detection, diagnosis, and treatment of cancer.[J]. Annual Review of Biomedical Engineering, 2013, 15(1):327-357.

[4] Dou Q, Chen H, Yu L, et al. Automatic Detection of Cerebral Microbleeds from MR Images via 3D Convolutional Neural Networks[J]. IEEE Transactions on Medical Imaging, 2016, 35(5):1182-1195.

[5] Anthimopoulos M, Christodoulidis S, Ebner L, et al. Lung Pattern Classification for Interstitial Lung Diseases Using a Deep Convolutional Neural Network[J]. IEEE Transactions on Medical Imaging, 2016, 35(5):1207-1216.

[6] Coroller T P, Grossmann P, Hou Y, et al. CT-based radiomic signature predicts distant metastasis in lung adenocarcinoma[J]. Radiotherapy & Oncology, 2015, 114(3):345-350.

[7] Aerts H J W L, Velazquez E R, Leijenaar R T H, et al. Decoding tumour phenotype by noninvasive imaging using a quantitative radiomics approach[J]. Nature Communications, 2014, 5:4006.
[8] Milletari F, Navab N, Ahmadi S A. V-Net: Fully Convolutional Neural Networks for Volumetric Medical Image Segmentation[J]. 2016:565-571.
[9] Ronneberger O, Fischer P, Brox T. U-Net: Convolutional Networks for Biomedical Image Segmentation[C]// International Conference on Medical Image Computing and Computer-Assisted Intervention. Springer, Cham, 2015:234-241.
[10] Dong H, Yang G, Liu F, et al. Automatic Brain Tumor Detection and Segmentation Using U-Net Based Fully Convolutional Networks[J]. 2017:506-517.
[11] Han Y, Ye J C. Framing U-Net via Deep Convolutional Framelets: Application to Sparse-View CT[J]. IEEE Transactions on Medical Imaging, 2018, 37(6):1418.
[12] Jin K H, Mccann M T, Froustey E, et al. Deep Convolutional Neural Network for Inverse Problems in Imaging[J]. IEEE Transactions on Image Processing, 2017, 26(9):4509-4522.
[13] Han Y S, Yoo J, Ye J C. Deep Residual Learning for Compressed Sensing CT Reconstruction via Persistent Homology Analysis[J]. arXiv preprint arXiv:1611.06391, 2016.
[14] Dalca A V, Guttag J, Sabuncu M R. Anatomical Priors in Convolutional Networks for Unsupervised Biomedical Segmentation[C]//Proceedings of the IEEE Conference on Computer Vision and Pattern Recognition. 2018: 9290-9299.
[15] Wachinger C, Reuter M, Klein T. DeepNAT: Deep convolutional neural network for segmenting neuroanatomy[J]. NeuroImage, 2018, 170: 434-445.
[16] Goodfellow I J, Pougetabadie J, Mirza M, et al. Generative Adversarial Networks[J]. Advances in Neural Information Processing Systems, 2014, 3:2672-2680.
[17] Radford A, Metz L, Chintala S. Unsupervised representation learning with deep convolutional generative adversarial networks[J]. arXiv preprint arXiv:1511.06434, 2015.
[18] Xu J, Xiang L, Liu Q, et al. Stacked Sparse Autoencoder (SSAE) for Nuclei Detection on Breast Cancer Histopathology Images[J]. IEEE Trans Med Imaging, 2016, 35(1):119-130.
[19] Gondara L. Medical image denoising using convolutional denoising autoencoders[J]. 2016:241-246.*arXiv preprint arXiv:1608.04667*
[20] Mirza M, Osindero S. Conditional Generative Adversarial Nets[J]. Computer Science, 2014:2672-2680.
[21] Dai W, Doyle J, Liang X, et al. SCAN: Structure Correcting Adversarial Network for Organ Segmentation in Chest X-rays[J]. arXiv preprint arXiv:1703.08770, 2017.
[22] Nie D, Trullo R, Lian J, et al. Medical image synthesis with context-aware generative adversarial networks[C]//International Conference on Medical Image Computing and Computer-Assisted Intervention. Springer, Cham, 2017: 417-425.
[23] Schlegl T, Seebck P, Waldstein S M, et al. Unsupervised Anomaly Detection with Generative Adversarial Networks to Guide Marker Discovery[J]. 2017:146-157.
[24] Ben-Cohen A, Klang E, Raskin S P, et al. Virtual PET Images from CT Data Using Deep Convolutional Networks: Initial Results[J]. 2017:49-57.
[25] Abdollahi H, Mostafaei S, Cheraghi S, et al. Cochlea CT radiomics predicts chemoradiotherapy induced sensorineural hearing loss in head and neck cancer patients: a machine learning and multi-variable modelling study[J]. Physica Medica, 2018, 45: 192-197.
[26] Acharya U R, Hagiwara Y, Sudarshan V K, et al. Towards precision medicine: from quantitative imaging to radiomics[J]. Journal of Zhejiang University-SCIENCE B, 2018, 19(1): 6-24.
[27] Constanzo J, Wei L, Tseng H H, et al. Radiomics in precision medicine for lung cancer[J]. Translational lung cancer research, 2017, 6(6): 635.
[28] Ning Z, Luo J, Li Y, et al. Pattern Classification for Gastrointestinal Stromal Tumors by Integration of Radiomics and Deep Convolutional Features[J]. IEEE Journal of Biomedical and Health Informatics, 2018.
[29] Wang K, Lu X, Zhou H, et al. Deep learning Radiomics of shear wave elastography significantly improved diagnostic performance for assessing liver fibrosis in chronic hepatitis B: a prospective multicentre study[J]. Gut, 2018: gutjnl-2018-316204.
[30] Saad M, Choi T S. Deciphering unclassified tumors of non-small-cell lung cancer through radiomics[J]. Computers in biology and medicine, 2017, 91: 222-230.
[31] Gevaert O, Xu J, Hoang C D, et al. Non-small cell lung cancer: identifying prognostic imaging biomarkers by leveraging public gene expression microarray datałmethods and preliminary results[J]. Radiology, 2012, 264(2): 387-396.
[32] Bakr, Shaimaa; Gevaert, Olivier; Echegaray, Sebastian; Ayers, Kelsey; Zhou, Mu; Shafiq, Majid; Zheng, Hong; Zhang, Weiruo; Leung, Ann; Kadoch, Michael; Shrager, Joseph; Quon, Andrew; Rubin, Daniel; Plevritis, Sylvia; Napel, Sandy.(2017). Data for NSCLC Radiogenomics Collection. The Cancer Imaging Archive.
[33] Aerts, Hugo J. W. L., Rios Velazquez, Emmanuel, Leijenaar, Ralph T. H., Parmar, Chintan, Grossmann, Patrick, Carvalho, Sara, Lambin, Philippe. (2015). Data From NSCLC-Radiomics-Genomics. The Cancer Imaging Archive.
[34] Johnson J, Alahi A, Fei-Fei L. Perceptual losses for real-time style transfer and super-resolution[C]//European Conference on Computer Vision. Springer, Cham, 2016: 694-711.
[35] Kingma D P, Ba J. Adam: A method for stochastic optimization[J]. arXiv preprint arXiv:1412.6980, 2014.
[36] Jin D, Xu Z, Tang Y, et al. CT-Realistic Lung Nodule Simulation from 3D Conditional Generative Adversarial Networks for Robust Lung Segmentation[J]. 2018.
[37] Dong S, Luo G, Wang K, et al. VoxelAtlasGAN: 3D Left Ventricle Segmentation on Echocardiography with Atlas Guided Generation and Voxel-to-voxel Discrimination[J]. arXiv preprint arXiv:1806.03619, 2018.